

Acquiring Measurement Matrices via Deep Basis Pursuit for Sparse Channel Estimation in mmWave Massive MIMO Systems

Pengxia Wu and Julian Cheng, *Senior Member, IEEE*

Abstract

For millimeter-wave (mmWave) massive multiple-input multiple-output (MIMO) systems, the down-link channel state information (CSI) acquisition causes large overhead in a frequency-division duplex system. The overhead of CSI acquisition can be substantially reduced when compressed sensing techniques are employed for channel estimations, owing to the sparsity feature in angular domain. Successful compressed sensing implementations depend on the choice of measurement matrices. Existing compressed sensing approaches widely adopt random matrices as measurement matrices. However, random measurement matrices have been criticized for their suboptimal reconstruction performances. In this paper, a novel data-driven approach is proposed to acquire the measurement matrix to address the shortcomings of random measurement matrices. Given a dataset, a generic framework of deep basis pursuit autoencoder is proposed to optimize the measurement matrix for minimizing reconstruction errors. Under this framework, two specific autoencoder models are constructed using deep unfolding, which is a model-based deep learning technique to acquire data-driven measurement matrices. Compared with random matrices, the acquired data-driven measurement matrices can achieve more accurate reconstructions using fewer measurements, and thus such a design can lead to a higher achievable rate for CSI acquisition in mmWave massive MIMO systems.

Index Terms

Channel estimation, CSI feedback, compressed sensing, deep learning, measurement matrix

P. Wu and J. Cheng are with the School of Engineering, The University of British Columbia, Kelowna, BC V1X 1V7, Canada (e-mail: pengxia.wu@ubc.ca, julian.cheng@ubc.ca). This work was in part submitted to IEEE Global Communications Conference, 2020.

I. INTRODUCTION

Millimeter-wave (mmWave) massive multiple-input multiple-output (MIMO) is considered as a promising technology for the next generation wireless communications due to its high capacity and ability to combat the small-scale fading of wireless channels [1]. In mmWave massive MIMO systems, accurate downlink channel state information (CSI) is essential for techniques such as the transmit beamforming [2] to obtain expected array-gains from large-scale antenna arrays [3]. For time-division duplex systems, downlink CSI acquisition is relatively unproblematic. Because base station (BS) can accurately and efficiently estimate the downlink channels from uplink pilots sent by the user equipments (UEs) based on channel reciprocity; the overhead of uplink pilots is affordable since it is only proportional to the number of UEs and is independent of the number of antennas of the BS. On the contrary, it is much more challenging for frequency division duplex (FDD) massive MIMO systems to acquire downlink CSI in a resource-efficient manner. The FDD massive MIMO system cannot exploit the channel reciprocity because the uplink and downlink channels occupy different spectrum bands. Consequently, downlink channels are often estimated at the UEs and then the UEs send back the estimated CSI to the BS. This downlink channel estimation and CSI feedback process consumes prohibitively high communication resources because both the overheads of downlink pilots and CSI feedback are proportional to the number of antennas at the BS, which is large in massive MIMO systems.

To reduce the overheads of CSI acquisition for FDD massive MIMO systems, one can exploit the channel sparsity in certain domains to develop the compressed sensing aided CSI acquisition schemes [4]–[9]. In compressed sensing aided CSI acquisition schemes, the overheads of downlink pilots and CSI feedback are no longer proportional to the number of antennas at the BS, but mostly depend on the sparsity level of the channel. Therefore, the overheads of downlink pilots and CSI feedback can be substantially reduced for channels having sparse characteristics. It is well known that the mmWave massive MIMO systems exhibit strong channel sparsity in the angular domain (or beamspace). Because a limited number of scattering clusters arrive at the high-dimensional antenna arrays with a small angular spread, the majority of channel components in beamspace are either zero or approximately zero, and only a few components have large magnitudes. Based on this sparsity feature of beamspace channels, compressed sensing techniques have shown promising advantages in developing beamspace channel estimation schemes [10]–[15] and compressed CSI feedback schemes [16]–[18] to reduce the overheads of downlink pilots

and CSI feedback for mmWave massive MIMO systems.

In compressed sensing aided CSI acquisition schemes, the unknown channels are characterized as high-dimensional vectors, and the channel vectors are sparse or can be represented as sparse vectors by certain basis. The sparse channel vectors are projected onto a compact subspace to obtain lower-dimensional measurements. Such a projection matrix is termed as measurement matrix and the projected subspace is the column space of the measurement matrix. Compressed sensing aided channel estimation reconstructs the high-dimensional sparse channel vectors from the lower-dimensional measurements, and the channel reconstruction quality highly depends on the chosen measurement matrix. Although existing compressed sensing aided CSI acquisition approaches have achieved considerable success and numerous channel reconstruction algorithms have been developed, they commonly adopt a random matrix as the measurement matrix. The random measurement matrix is a matrix having the elements produced by a random variable following a given distribution. The random measurement matrix performs random projections and cannot fully exploit underlying channel structures. These randomized measurement matrices, drawn from Gaussian or Bernoulli distribution, are not optimal for all channel realizations. Thus, they have unsatisfactory reconstruction performance, especially when the number of measurements is insufficient [19]. While increasing the number of measurements will ultimately improve recovery accuracy, this approach is undesirable. It has been pointed out that the measurement matrix should be optimized to reduce the least number of measurements required for accurate sparse channel reconstructions [4], [17], [19], [20]. An alternative to the random matrix is to design a deterministic matrix that satisfies the restricted isometry property (RIP) [21]–[23]. However, it is an NP-hard problem to determine whether a matrix satisfies the RIP [19]. Till this end, the construction of deterministic measurement matrix still lacks explicit guidelines [4]. Some deterministic measurement matrices were designed for specific applications in an ad hoc manner [24], [25], and they do not perform well for different channel realizations.

In this paper, we propose a data-driven approach to acquire the measurement matrix for sparse CSI acquisitions using deep unfolding, which is a model-based deep learning technique [26]. Deep unfolding is an attractive way to build non-blackbox deep learning architectures from model-based iterative algorithms. More interestingly, we show that the data-driven measurement matrices, which are acquired from the well-trained deep learning models, have excellent reconstruction performances in the classical model-based sparse recovery algorithms performed by linear programming solvers. In our approach, we propose a generic framework of deep basis

pursuit autoencoder (BP-AE) to learn automatically an optimal measurement matrix via training on the given beamspace channel dataset. We construct two specific autoencoder models, which mimic the compressed sensing process including the linear sensing and basis pursuit sparse reconstruction [27]. The designed autoencoders are parameterized by the measurement matrix as trainable variables, so that the measurement matrices can be optimized via backpropagating to minimize the input-output reconstruction errors when training the autoencoders on given dataset. The acquired data-driven measurement matrix can be applied to designing the training pilots or compressing the feedback CSI for downlink FDD mmWave massive MIMO systems. Although the data-driven measurement matrix has been investigated for the nonnegative datasets having explicit structural features [28], it is not a straight-forward extension in a general problem setting of CSI acquisitions. Considering the fact that the data preprocessing is infeasible in practical implementations of channel estimations, a general deep learning architecture is required to acquire the data-driven measurement matrices for sparse channel reconstructions. At last, it is worth to mention the difference of our work with the recent research on deep learning based CSI acquisitions [29]–[36]. While these works have successfully developed end-to-end deep learning models for channel estimations, they do not adopt compressed sensing techniques and do not consider designing the measurement matrix. Major contributions of this paper are summarized as follows:

- We propose a novel data-driven method for acquiring measurement matrix, and this method provides a better alternative to random matrices for compressed sensing aided beamspace channel estimation and CSI feedback schemes. Since the acquired measurement matrices are data-driven, they can exploit the underlying structural features beyond simple sparsity of given beamspace channel dataset. Consequently, the acquired data-driven measurement matrices can achieve better reconstruction performance and use fewer measurements than random matrices.
- We further improve the data-driven measurement matrices by introducing auxiliary features such as the nonnegativity in the training data. These improved measurement matrices are obtained by extending the proposed autoencoders to acquire the data-driven measurement matrices for the nonnegative sparse vectors, and these vectors are the concatenations of positive and negative parts of original sparse vectors. Although the extended measurement matrices have double columns, they provide further improved reconstruction performances.

- We propose a generic framework of deep BP-AE, which embeds the compressed sensing algorithm into an autoencoder architecture so that the forward and backward computations within the neural network are fully interpretable. Through mimicking the processes of linear sensing and nonlinear basis pursuit recovery, the feed-forward computation is guided to reproduce the input at the output. By treating the measurement matrix as trainable variables, the back-forward computation optimizes the measurement matrix via back-propagation to minimize the reconstruction errors.
- We design two model-based decoders using deep unfolding that transforms the traditional iterative basis pursuit algorithm into a stack of deep neural networks. The measurement matrices are acquired by jointly training the linearly-sensing encoder and the deep-unfolding decoders. Interestingly, the acquired data-driven measurement matrices perform well in the classical model-based sparse recoveries by linear programming solver. This result reveals a potential application of deep neural networks to optimize the parameters of classical model-based algorithms for performance improvement.

The remainder of this paper are organized as follows. Section II presents the system model for beamspace channel estimation and CSI feedback, and this section also introduces the issue of designing measurement matrix. Section III proposes a generic compressed sensing autoencoder framework. Then, this section also proposes two specific autoencoder models to acquire the data-driven measurement matrix for beamspace channel vectors. Furthermore, this section further proposes extension models to acquire the measurement matrices having double columns to improve performance. Section IV presents numerical results, followed by the conclusions in Section V.

Notations: This paper adopts the following notations. Column vectors and matrices are denoted by lower-case and upper-case boldface letters, respectively; $(\cdot)^T$, $(\cdot)^H$ and $(\cdot)^\dagger$ denote the transpose, conjugate transpose and the pseudo-inverse, respectively; $\mathbb{C}^{m \times n}$ is the set of $m \times n$ matrices having complex-valued entries; $\mathbb{R}^{m \times n}$ is the set of $m \times n$ matrices with real-valued entries; $\mathbb{E}[\cdot]$ represents expectation operator; $(\cdot)_i$ and $(\cdot)_{i,j}$ represent the i th element of a vector and the (i, j) th element of a matrix, respectively; $\|\cdot\|_p$ represents the ℓ_p -norm of a vector.

II. SYSTEM MODEL

A. Sparse Beamspace Channel for mmWave Massive MIMO Systems

We consider a downlink mmWave massive MIMO system, where the BS is equipped with N antennas and the user equipment (UE) is equipped with a single antenna. For the narrowband block fading channel, we use the vector $\mathbf{h}_s \in \mathbb{C}^N$ to denote the spatial-domain channel between the BS and the UE. The Saleh-Valenzuela channel model is adopted for the mmWave channels, and the spatial-domain channel vector \mathbf{h}_s is given by [12]

$$\mathbf{h}_s = \sqrt{\frac{N}{N_p}} \sum_{l=1}^{N_p} \beta^{(l)} \boldsymbol{\alpha}(\phi^{(l)}) \quad (1)$$

where N_p is the number of scattering clusters; $l = 1$ is the index for the line-of-sight path; $2 \leq l \leq N_p$ is the index for non-line-of-sight paths; $\beta^{(l)}$ is the complex path gain; $\boldsymbol{\alpha}(\phi^{(l)})$ is the corresponding array steering vector that contains a list of complex spatial sinusoids representing the relative phase shifts of the incident far-field waveform across the array elements. For the N -element uniform linear array, the array steering vector $\boldsymbol{\alpha}(\phi^{(l)})$ is given by

$$\boldsymbol{\alpha}(\phi^{(l)}) = \frac{1}{\sqrt{N}} [1, e^{-j2\pi\phi^{(l)}}, \dots, e^{-j2\pi\phi^{(l)}(N-1)}]^T \quad (2)$$

where $\phi^{(l)}$ denotes the spatial direction of the l th path, and it is related to the physical angle $\theta^{(l)}$ by $\phi^{(l)} = \frac{d}{\lambda} \sin \theta^{(l)}$ for $-\frac{1}{2} \leq \phi^{(l)} \leq \frac{1}{2}$ and $-\frac{\pi}{2} \leq \theta^{(l)} \leq \frac{\pi}{2}$, where λ is the wavelength of mmWave, and $d = \frac{\lambda}{2}$ is the antenna spacing.

The spatial channel vector \mathbf{h}_s in (1) can be transformed into the beamspace channel vector \mathbf{h} by [37]

$$\mathbf{h} = \mathbf{U} \mathbf{h}_s \quad (3)$$

where \mathbf{U} denotes the DFT matrix having the size $N \times N$, and it can be expressed using a set of orthogonal array steering vectors as

$$\mathbf{U} = [\boldsymbol{\alpha}(\phi_1), \boldsymbol{\alpha}(\phi_2), \dots, \boldsymbol{\alpha}(\phi_N)]^H \quad (4)$$

where $\phi_m = \frac{1}{N}(m - \frac{N+1}{2})$ for $m = 1, 2, \dots, N$ is the spatial direction predefined by the array having half-wavelength spaced antennas. The beamspace sparsity is an important feature of mmWave massive MIMO channels. From (3) and (4), the i th element of \mathbf{h} is

$$\mathbf{h}_{(i)} = \sum_{l=1}^{N_p} \alpha_l \boldsymbol{\alpha}^H(\phi_i) \boldsymbol{\alpha}(\phi^{(l)}) \quad (5)$$

where $\mathbf{h}_{(i)}$ denotes the i th element of vector \mathbf{h} . Eq. (5) indicates that the beamspace channel element $\mathbf{h}_{(i)}$ is the assemble of all the channel gains for the paths whose angle of departures (AoDs) fall into the virtual angular bin represented by the spatial direction ϕ_i . The limited number N_p of scattering clusters indicates a limited number of spatial directions $\phi^{(l)}$ in (5), following a fact that only a small number of elements are nonzero in the beamspace channel vector \mathbf{h} . In practice due to the limited resolution of virtual angular bins, the mismatches often happen between the real AoDs $\phi^{(l)}$ for $1 \leq l \leq N_p$ and the predefined angles ϕ_i for $1 \leq i \leq N$ of the virtual angular bins. This phenomenon is known as the power leakage, which causes the beamspace channels being not exactly sparse. However, the power leakage is negligible in the massive MIMO systems having hundreds of antenna elements. In this situation, the energy (square sum) of a few large-valued elements can capture the most of the channel energy $\|\mathbf{h}\|_2^2$, and thus we say the beamspace channel is approximately sparse or compressible [3].

B. Downlink Sparse Channel Acquisition: Channel Estimation and Feedback

For the pilot-aided downlink channel estimation, the BS transmits the known pilots \mathbf{P} to the UEs. The received pilot symbols at the UE can be expressed as [4]

$$\mathbf{r} = \mathbf{P}\mathbf{h}_s + \mathbf{w} \quad (6)$$

where $\mathbf{r} \in \mathbb{C}^M$ is the received pilots; $\mathbf{P} \in \mathbb{C}^{M \times N}$ is the pilot matrix transmitted over M time slots; $\mathbf{h}_s \in \mathbb{C}^N$ is the spatial-domain channel vector; \mathbf{w} is the received noise vector and $\mathbf{w} \sim \mathcal{CN}(0, \sigma_n^2 \mathbf{I})$. The conventional linear reconstruction methods, such as the linear minimum mean square error or the least squares, require $M \geq N$ for robust estimation of \mathbf{h}_s , where M indicates the length of pilot sequences and N is the number of BS antennas. For massive MIMO systems having a large number of antennas, the requirement on pilot length will cause prohibitive spectral occupancy and high computation complexity. For this reason, it is attractive to develop compressed sensing aided beamspace channel estimation schemes. According to the relationship between the spatial-domain channel \mathbf{h}_s and the beamspace channel \mathbf{h} in (3), the channel vector \mathbf{h}_s in (6) can be replaced by $\mathbf{h}_s = \mathbf{U}^H \mathbf{h}$ and the received pilot symbols in (6) can be rewritten as

$$\mathbf{r} = \mathbf{P}\mathbf{U}^H \mathbf{h} + \mathbf{w}. \quad (7)$$

Let $\mathbf{A} = \mathbf{P}\mathbf{U}^H$, eq. (7) can be expressed as

$$\mathbf{r} = \mathbf{A}\mathbf{h} + \mathbf{w}. \quad (8)$$

Eq. (8) is a typical compressed sensing formulation, where $\mathbf{r} \in \mathbb{C}^M$ is the observation vector, also termed as the measurement vector; $\mathbf{A} \in \mathbb{C}^{M \times N}$ is the measurement matrix; $\mathbf{h} \in \mathbb{C}^N$ is a sparse vector; \mathbf{w} is the noise vector. According to the compressed sensing theory, the sparse beamspace channel vector \mathbf{h} can be estimated accurately from the measurements \mathbf{r} for $M \ll N$, thus the overheads of downlink pilots and CSI feedback can be largely reduced. Based on (8), we consider two application scenarios of the FDD downlink CSI acquisitions. In the first scenario, the BS transmits the pilots $\mathbf{P} \in \mathbb{C}^{M \times N}$; the UE sends back the received measurements \mathbf{r} to the BS; the sparse beamspace vector \mathbf{h} is reconstructed at the BS from the measurements \mathbf{r} . In this channel estimation scenario, the matrix $\mathbf{A} = \mathbf{P}\mathbf{U}^H$ is the measurement matrix. Designing the measurement matrix \mathbf{A} is equivalent to designing the pilot matrix \mathbf{P} . In the second scenario, we consider the CSI feedback problem and assume that the ideal CSI is already known at the UE. The UE uses the measurement matrix \mathbf{A} to compress the beamspace channel vector \mathbf{h} , then it sends back the compressed measurements \mathbf{r} to the BS; the BS performs recovery algorithms to reconstruct the beamspace channel vector \mathbf{h} . For both application scenarios, we need to reconstruct the beamspace channel vector \mathbf{h} from the measurements \mathbf{r} as described by the underdetermined linear equation (8). The reconstruction quality of beamspace channel vector \mathbf{h} highly depends on the property of the measurement matrix \mathbf{A} in (8).

In this paper, we adopt the real-valued measurement matrix denoted by $\Phi \in \mathbb{R}^{M \times N}$. Thus, the real and imaginary parts of all complex variables in (8) can be dealt with separately, that is

$$\begin{aligned}\Re(\mathbf{r}) &= \Phi \cdot \Re(\mathbf{h}) + \Re(\mathbf{w}) \\ \Im(\mathbf{r}) &= \Phi \cdot \Im(\mathbf{h}) + \Im(\mathbf{w})\end{aligned}\tag{9}$$

where $\Re(\cdot)$ and $\Im(\cdot)$ denote the real and imaginary part of a complex vector. Eq. (9) implies that we can simply treat a complex channel vector \mathbf{h} as two real-form vectors. Therefore, we can uniquely express (9) using the underdetermined linear equation

$$\mathbf{y} = \Phi \mathbf{x} + \mathbf{n}\tag{10}$$

where $\mathbf{y} \in \mathbb{R}^M$ denotes the measurements; $\Phi \in \mathbb{R}^{M \times N}$ is the measurement matrix that we aim to design; $\mathbf{x} \in \mathbb{R}^N$ represents the sparse vector to be estimated; $\mathbf{n} \in \mathbb{R}^M$ is the Gaussian noise vector and $\mathbf{n} \sim \mathcal{N}(0, \sigma_n^2 \mathbf{I})$. In the remaining of this paper, we use \mathbf{x} to represent uniquely the samples in the dataset consisting of real and imaginary parts of the beamspace channel vectors. Since a complex channel vector \mathbf{h} can be equivalently regarded as two real-form vectors $\mathbf{x} = \Re(\mathbf{h})$

and $\mathbf{x} = \Im(\mathbf{h})$, we do not make particular distinctions for the real and imaginary parts of \mathbf{h} and uniquely refer \mathbf{x} as the sparse channel vector.

To reconstruct the sparse channel vector \mathbf{x} successfully from the measurements \mathbf{y} , we need to design the measurement matrix Φ appropriately such that the projection $\Phi\mathbf{x}$ of vector \mathbf{x} will retain as much information of \mathbf{x} as possible. The property of a measurement matrix can be characterized by some conditions such as the RIP [38], mutual incoherence property (known as MIP [39]) and null space property (known as NSP [40]). It has been proved that the matrices Φ satisfying these conditions are guaranteed to reconstruct the sparse vector \mathbf{x} exactly from the projection $\Phi\mathbf{x}$ [41]. However, the computation is too complicated to determine whether a given matrix satisfies these conditions. Fortunately, a randomly generated matrix Φ has been shown satisfying these conditions with a high probability; moreover, this probability increases exponentially with the dimension of measurements [27]. In other words, the reconstruction can be asymptotically accurate by adopting random matrices with sufficient measurements, i.e., for a sufficiently large value of M . Therefore, the random matrices are default choices for compressed sensing with a sufficiently large value of M . The entries of such a random measurement matrix can be independently drawn from a distribution such as the Gaussian distribution or symmetric Bernoulli distribution. The randomly chosen rows of a Fourier matrix or an orthonormal matrix can also compose a measurement matrix. However, these random matrices cannot exploit the underlying channel structures and their reconstruction performances are found unsatisfactory at the low compressed dimension M . Since we desire to use fewer measurements to accomplish accurate reconstructions, it is important to reduce the least number of measurements required for accurate reconstructions when designing a measurement matrix. We will show that the data-driven measurement matrices acquired by our proposed autoencoders provide a promising alternative.

III. LEARNING A MEASUREMENT MATRIX BY DEEP BP-AE

In this section, we propose a general framework of deep BP-AE for measurement matrix optimization. Under this framework, we propose two autoencoder models whose decoders are constructed by the deep unfolding of the iterations of basis pursuit sparse reconstruction. In addition, we extend the proposed two autoencoder models for learning the measurement matrix having double columns, which can further improve reconstruction performance.

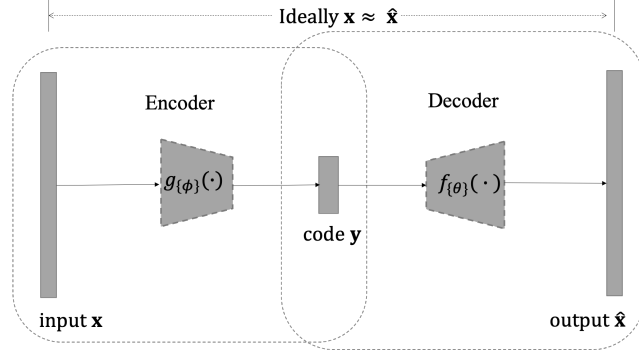


Fig. 1: The schematic structure of an autoencoder

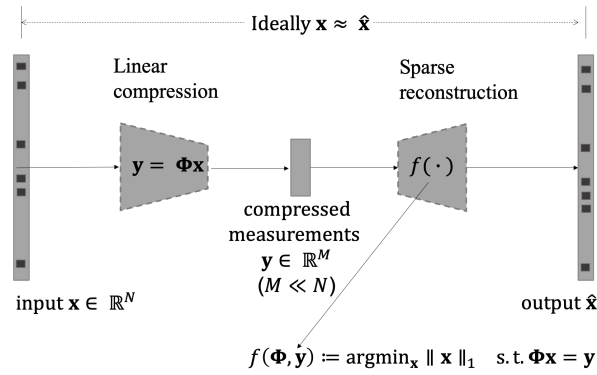


Fig. 2: Framework of deep BP-AE

A. Deep BP-AE Framework

Both an autoencoder and a compressed sensing process have similar “encoding-decoding” structure such that these two techniques can be integrated to design a particular kind of model-based autoencoder. The autoencoder is an unsupervised learning technique in deep learning, and it is a neural network that can be trained to reproduce its input at the output through a stack of hidden layers which describes a code to represent the input. The aim of an autoencoder is to learn the latent representation (code) for a set of data, typically for dimensionality reduction or feature extraction. As shown in Fig. 1, an autoencoder structure consists of two main parts: an encoder that maps the input into the code, i.e., $\mathbf{y} = g_{\{\phi\}}(\mathbf{x})$, and a decoder that maps the code to a reconstruction of the original input, i.e., $\hat{\mathbf{x}} = f_{\{\theta\}}(\mathbf{y})$. Here, we use the functions $g(\cdot)$, $f(\cdot)$ to represent the nonlinear transformations of the encoder and decoder, and $\{\phi\}$, $\{\theta\}$ represent the trainable parameter sets of the encoder and decoder.

Similar to autoencoder, a complete compressed sensing process involves two phases: the

linear encoding (or compression) and the nonlinear decoding (or sparse recovery). In the linear compression phase, the measurement matrix is used to project the sparse vectors onto the subspace and obtain the measurements that can best represent the sparse vectors. In the sparse recovery phase, the measurement matrix participates in the recovery algorithm computations. The basis pursuit, an ℓ_1 -minimization optimization, is one of sparse recovery methods. Thus, a complete compressed sensing process can be interpreted as a special autoencoder consisting of a linear encoder and a sparse-reconstruction decoder, and the “encoder” and the “decoder” can be explicitly defined as

$$g(\cdot) := \Phi \mathbf{x},$$

$$f(\cdot) := \underset{\mathbf{x}}{\operatorname{argmin}} \|\mathbf{x}\|_1 \quad \text{s.t. } \Phi \mathbf{x} = \mathbf{y}$$

where the decoder performs an ℓ_1 -minimization sparse reconstruction, which is also known as the basis pursuit in signal processing. Based on this observation, we propose a framework of the deep BP-AE, which mimicks the processes of linear sensing and basis pursuit under an autoencoder architecture. As shown in Fig. 2, the encoder performs linear sensing or compression, and the decoder solves the basis pursuit problem for sparse reconstruction.

To optimize the measurement matrix, we parameterize the deep BP-AE with measurement matrix Φ as trainable parameters. Similar to a standard autoencoder that optimizes the trainable parameters $\{\phi\}$ and $\{\theta\}$ through training with given dataset by backpropagation, the BP-AE can also optimize the measurement matrix Φ in the same way. The training objective is to minimize the input-output reconstruction error, and the optimizer can use standard deep learning techniques such as the stochastic gradient descent (SGD) algorithm based on backpropagation [42]. The proposed deep BP-AE structure is easy to understand. More specifically, from the viewpoint of forward computation, the autoencoder performs the linear dimensionality reduction jointly with basis pursuit sparse reconstruction, such that it can be regarded as a complete compressed sensing process. From the viewpoint of backward propagation, the autoencoder back propagates and minimizes the reconstruct errors using SGD, such that it can be regarded as an SGD optimizer for the measurement matrix.

B. Architecture of Deep BP-AE

The overall network architecture of deep basis pursuit autoencoder is shown in Fig. 3. The encoder is simply a linear fully-connected layer $\mathbf{y} = \Phi \mathbf{x}$ without activation function. The

measurements \mathbf{y} is the input of the decoder, and the first-layer decoder is $\mathbf{x}^{(1)} = \Phi^T \mathbf{y}$. From the first-layer decoder $\mathbf{x}^{(1)}$ to the last-layer decoder that outputs the reconstruction $\hat{\mathbf{x}}$, the network is a stack of iterative updates $\mathbf{x}^{(t+1)} = f_{\Phi}(\mathbf{x}^{(t)}, \mathbf{y})$ for $1 \leq t \leq L$. These iterative updates are defined basically according to an iterative solution of basis pursuit for sparse reconstruction. This method of using an iterative solution to construct a deep neural network is called deep unfolding [26]. Deep unfolding regards each step of iterations as a single layer of neural network to transform a traditional iterative algorithm into a stack layers of neural networks. Unlike the traditional iterative algorithms having predefined stopping conditions and manually tuning parameters, the unfolding neural networks have a fixed number of iterative layers and the trainable parameters are learned from the training data. Before discussing details of the unfolding architecture of decoder, we need to derive an iterative solution of the basis pursuit for sparse reconstruction.

The sparse reconstruction is an ℓ_0 -norm minimization optimization problem ¹

$$\min_{\mathbf{x}} \|\mathbf{x}\|_0 \quad \text{s.t.} \quad \Phi \mathbf{x} = \mathbf{y} \quad (11)$$

where $\|\cdot\|_0$ represents the zero-norm, which is defined as the number of nonzero elements in a vector. The combinatorial optimization problem (11) is NP-hard [43]. A common method is to relax the problem (11) into a convex ℓ_1 -minimization optimization problem, which is also known as basis pursuit as

$$\min_{\mathbf{x}} \|\mathbf{x}\|_1 \quad \text{s.t.} \quad \Phi \mathbf{x} = \mathbf{y} \quad (12)$$

where $\|\cdot\|_1$ represents the one-norm, which is defined as the sum of the absolute values of all elements in a vector. We adopt the projected subgradient descent to solve the problem (12) and the update is given by [44]

$$\mathbf{x}^{(t+1)} = Proj(\mathbf{x}^{(t)} - \alpha_t \cdot \text{sign}(\mathbf{x}^{(t)})) \quad (13)$$

where t indicates the t th update for $t > 0$; α_t is the step size; $\text{sign}(\cdot)$ represents the Signum function which is the subgradient of $\|\cdot\|_1$; $Proj(\cdot)$ represents the projection operation onto the convex set $\{\mathbf{x}' : \Phi \mathbf{x}' = \mathbf{y}\}$. The projection of a vector \mathbf{z} onto the set $\{\mathbf{x}' : \Phi \mathbf{x}' = \mathbf{y}\}$ has the following closed-form solution

$$Proj(\mathbf{z}) = \mathbf{z} + \Phi^\dagger(\mathbf{y} - \Phi \mathbf{z}) \quad (14)$$

¹We consider the noise-less case, and the extension to noisy case is left for the future work.

where $\Phi^\dagger = \Phi^T(\Phi\Phi^T)^{-1}$ is the Moore-Penrose pseudo-inverse of Φ . We substitute $\mathbf{z} = \mathbf{x}^{(t)} - \alpha_t \cdot \text{sign}(\mathbf{x}^{(t)})$ from (13) into the projection operation (14) and obtain the t th-step update as

$$\mathbf{x}^{(t+1)} = \mathbf{x}^{(t)} + \Phi^\dagger(\mathbf{y} - \Phi\mathbf{x}^{(t)}) - \alpha_t(\mathbf{I} - \Phi^\dagger\Phi) \cdot \text{sign}(\mathbf{x}^{(t)}). \quad (15)$$

Given a proper starting point $\mathbf{x}^{(1)}$, step size α_t and stop condition, the update (15) can be regarded a simple iterative sparse reconstruction algorithm for reconstructing $\hat{\mathbf{x}}$. We unfold this iteration algorithm for constructing the unknown decoder of the deep BP-AE in Fig. 3. More precisely, we use the update (15) to guide the forward computations of the $(t + 1)$ th-layer decoder with making the following adjustments:

- The pseudo-inverse Φ^\dagger is replaced by the transpose Φ^T to release intensive computations.
- The step size parameter is set as $\alpha_t = \alpha/t$ according to the diminishing step size rule [44].

In this way, the update (15) becomes

$$\mathbf{x}^{(t+1)} = \mathbf{x}^{(t)} + \Phi^T\mathbf{y} - \Phi^T\Phi\mathbf{x}^{(t)} - (\alpha/t)(\mathbf{I} - \Phi^T\Phi) \cdot \text{sign}(\mathbf{x}^{(t)}). \quad (16)$$

The computational flow of the $(t + 1)$ th-layer decoder $\mathbf{x}^{(t+1)} = f_\Phi(\mathbf{x}^{(t)}, \mathbf{y})$ for $1 \leq t \leq L - 1$ would be defined basically based on the update (16). By treating the measurements \mathbf{y} in (16) in different ways, we can define two decoders with different computation graphs². Then, by implementing the two specific decoders in the deep BP-AE architecture shown in Fig. 3, we build two autoencoder models namely the basis pursuit simplified autoencoder (BP-SAE) and the basis pursuit generic autoencoder (BP-GAE).

BP-SAE decoder: By substituting $\mathbf{y} = \Phi\mathbf{x}^{(t)}$ in update (16) we obtain

$$\mathbf{x}^{(t+1)} = \mathbf{x}^{(t)} - (\alpha/t)(\mathbf{I} - \Phi^T\Phi) \cdot \text{sign}(\mathbf{x}^{(t)}) \quad (17)$$

which represents the t th-layer computation of the BP-SAE decoder. The computation graph of iteration (17) for the t th-layer decoder of BP-SAE is shown in Fig. 4.

BP-GAE decoder: By treating $\mathbf{y} = \Phi\mathbf{x}^{(t-1)}$, the update (16) becomes

$$\mathbf{x}^{(t+1)} = \mathbf{x}^{(t)} + \Phi^T\Phi\mathbf{x}^{(t-1)} - \Phi^T\Phi\mathbf{x}^{(t)} - (\alpha/t)(\mathbf{I} - \Phi^T\Phi) \cdot \text{sign}(\mathbf{x}^{(t)}). \quad (18)$$

The iteration (18) represents the computation of the t th-layer decoder of the BP-GAE. The computation graph of iteration (18) for the t th-layer decoder of BP-GAE is shown in Fig. 5.

²In deep learning, the computation graph is used to represent a math function in the language of graph theory for visualizing the computation flow.

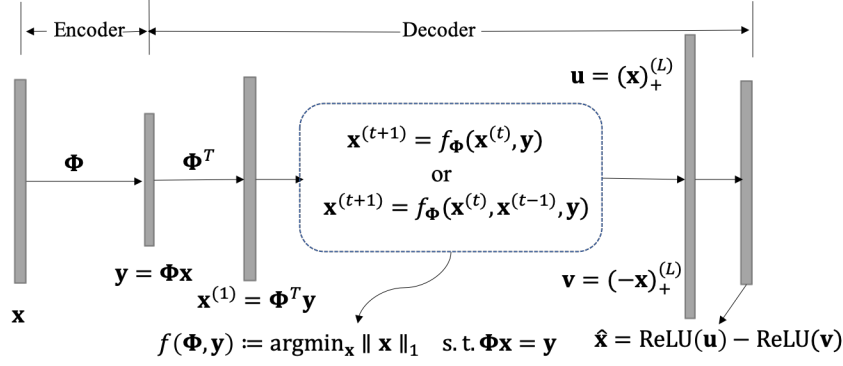


Fig. 3: Structure diagram of deep BP-AE

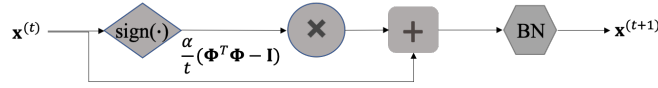


Fig. 4: Computation graph of BP-SAE decoder for $\mathbf{x}^{(t+1)} = f_{\Phi}(\mathbf{x}^{(t)}, \mathbf{y})$ for $0 \leq t \leq L$; the module BN represents batch normalization

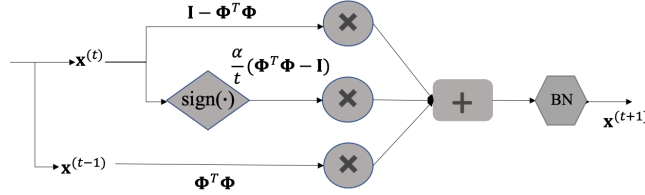


Fig. 5: Computation graph of BP-GAE decoder for $\mathbf{x}^{(t+1)} = f_{\Phi}(\mathbf{x}^{(t)}, \mathbf{x}^{(t-1)}, \mathbf{y})$ for $0 \leq t \leq L$; the module BN represents batch normalization

The benefit of treating \mathbf{y} as $\Phi \mathbf{x}^{(t-1)}$ comes from the role of $\mathbf{x}^{(t-1)}$, which can be understood as introducing the residual learning unit [45] to improve the autoencoder performance.

At the output layer, we represent the channel vector $\mathbf{x}^{(L)}$ in the L th-layer decoder using the difference of its positive and negative part, and add the ReLU³ activation function for the output.

³ReLU stands for rectified linear unit, and it is a type of activation function. Mathematically, it is defined as $\operatorname{ReLU}(x) = \max(0, x)$ when x is a scale. When the input is a vector, $\operatorname{ReLU}(\cdot)$ is applied in an element-wise manner.

We represent

$$\begin{aligned}\mathbf{x}^{(L)} &= \mathbf{u} - \mathbf{v} \\ \mathbf{u} &= \mathbf{x}_+^{(L)}, \mathbf{v} = (-\mathbf{x}^{(L)})_+\end{aligned}\quad (19)$$

where $(\cdot)_+$ denotes the positive-taking operator that retains the positive components of a vector and sets other elements be zeros. More specifically, $\mathbf{x}_+^{(L)}$ indicates for each element we have $(\mathbf{x}_+^{(L)})_i = \max\{\mathbf{x}_i, 0\}$ for $i = 1, \dots, N$, and $(-\mathbf{x}^{(L)})_+$ indicates for each element we have $((-\mathbf{x}^{(L)})_+)_i = \max\{-\mathbf{x}_i^{(L)}, 0\}$ for $i = 1, \dots, N$. With the ReLU activation functions operating on the nonnegative vectors \mathbf{u} and \mathbf{v} , the output layer of the decoder can be represented as

$$\hat{\mathbf{x}} = \text{ReLU}(\mathbf{u}) - \text{ReLU}(\mathbf{v}) \quad (20)$$

where $\hat{\mathbf{x}}$ represents the final reconstructed channel vector at the output of the autoencoder. The ℓ_1 -AE proposed in [28], [46] is a special case of BP-SAE when the data \mathbf{x} is nonnegative, so that the variable splitting (19) needs not to implement.

The loss function of the autoencoders is defined as the mean square ℓ_2 -error (MSE) between input samples \mathbf{x} and reconstructed output vectors $\hat{\mathbf{x}}$,

$$L(\mathbf{x}, \hat{\mathbf{x}}) = \frac{1}{n} \sum_{i=1}^n \|\mathbf{x} - \hat{\mathbf{x}}\|_2^2 \quad (21)$$

where n is the number of training samples. The encoder and decoder of the autoencoder are jointly optimized on given dataset to minimize the reconstruction error (21). The trainable variables are $\{\Phi, \alpha\}$. During the training, the measurement matrix Φ as the trainable variables are automatically tuned to be optimal based on the given dataset. Therefore, the obtained measurement matrix is data-driven and can adapt to the dataset features. After training, the optimal data-driven measurement matrix $\Phi \in \mathbb{R}^{M \times N}$ can be extracted from the well-trained autoencoder models.

C. Extension Models for the Data-Driven Measurement Matrices having Double Columns

Normally, the data-driven measurement matrix acquired by BP-SAE or BP-GAE has the dimension $M \times N$, where M is the compressed dimension and N is the dimension of sparse vectors. If we perform the variable split starting from the encoder, we can slightly modify the BP-SAE and BP-GAE for acquiring the measurement matrices with dimension $M \times 2N$.

We perform variable splitting at the encoder. The channel vector \mathbf{x} is represented as the difference between its positive part and negative part, i.e., $\mathbf{x} = \mathbf{u} - \mathbf{v}$, where

$$\mathbf{u} = \mathbf{x}_+, \quad \mathbf{v} = (-\mathbf{x})_+, \quad (22)$$

where \mathbf{x}_+ denotes retaining the positive components of the vector \mathbf{x} and setting the other elements be zeros, that is $(\mathbf{x}_+)_i = \max\{\mathbf{x}_i, 0\}$ for $i = 1, \dots, N$, and $(-\mathbf{x})_+$ denotes retaining the positive components of the vector $-\mathbf{x}$ and setting the other elements be zeros, that is $((-\mathbf{x})_+)_i = \max\{-\mathbf{x}_i, 0\}$ for $i = 1, \dots, N$. The problem (12) can be rewritten as

$$\begin{aligned} \min_{\mathbf{h}} \quad & \|(\mathbf{u} - \mathbf{v})\|_1 \\ \text{s.t.} \quad & \Phi(\mathbf{u} - \mathbf{v}) = \mathbf{y}, \quad \mathbf{u} \geq \mathbf{0}, \quad \mathbf{v} \geq \mathbf{0}. \end{aligned} \quad (23)$$

Then we use the double-sized channel vector $\tilde{\mathbf{x}}$ to denote the concatenating of \mathbf{u} and \mathbf{v} , i.e., $\tilde{\mathbf{x}} = [\mathbf{u}^T, \mathbf{v}^T]^T$, and rewrite the problem (23) as

$$\min_{\tilde{\mathbf{x}}} \|\tilde{\mathbf{x}}\|_1 \quad \text{s.t.} \quad [\Phi, -\Phi]\tilde{\mathbf{x}} = \mathbf{y}, \tilde{\mathbf{x}} \geq \mathbf{0}. \quad (24)$$

We use the double-column sized matrix $\tilde{\Phi} \in \mathbb{R}^{M \times 2N}$ to replace the matrix $[\Phi, -\Phi]$, where $\Phi \in \mathbb{R}^{M \times N}$, and the problem (24) can be simplified to be

$$\min_{\tilde{\mathbf{x}}} \|\tilde{\mathbf{x}}\|_1 \quad \text{s.t.} \quad \tilde{\Phi}\tilde{\mathbf{x}} = \mathbf{y}, \tilde{\mathbf{x}} \geq \mathbf{0}. \quad (25)$$

The problem (25) is an equivalent expression with the problem (12) with the following two distinctions. First, the variables $\tilde{\mathbf{x}}$ and $\tilde{\Phi}$ in problem (25) are double-sized compared with \mathbf{x} and Φ in the problem (12). Second, the problem (25) has an auxiliary nonnegativity constraint $\tilde{\mathbf{x}} \geq \mathbf{0}$. We apply the autoencoders BP-SAE and BP-GAE on the intermediate variables $\tilde{\mathbf{x}}$ to acquire the measurement matrix $\tilde{\Phi}$. The corresponding modified autoencoders are named as BP-SAEcat and BP-GAEcat, and their structure diagrams are shown in Fig. 6 and Fig. 7 respectively. Compared with the data-driven measurement matrix $\Phi \in \mathbb{R}^{M \times N}$ acquired by BP-SAE and BP-GAE, the data-driven measurement matrix $\tilde{\Phi} \in \mathbb{R}^{M \times 2N}$ acquired by the extension models BP-SAEcat and BP-GAEcat will be shown to have improved reconstruction performance. One reason is that the larger-size $\tilde{\Phi}$ has more variables to be optimized, which means higher degrees of freedom for the neural network. Another reason is that the introduced nonnegativity constraint $\tilde{\mathbf{x}} \geq \mathbf{0}$ provides an obvious feature that can be fit by the neural network, so that the corresponding adaptations to this data feature can be automatically adjusted on the measurement matrix $\tilde{\Phi}$.

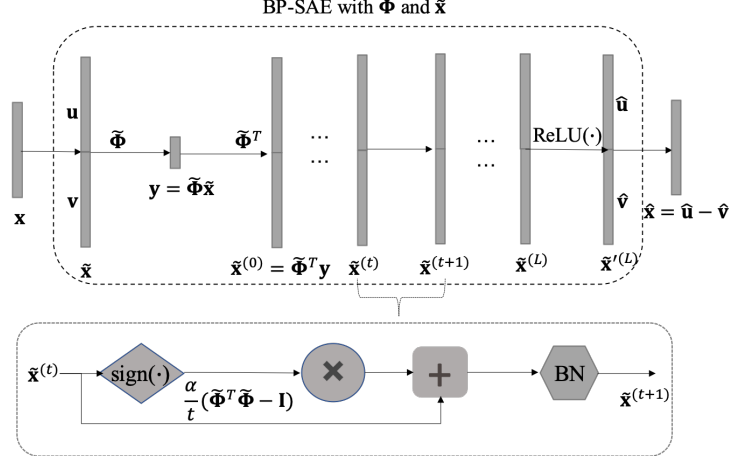


Fig. 6: Structure diagram of BP-SAEcat; the module BN represents batch normalization

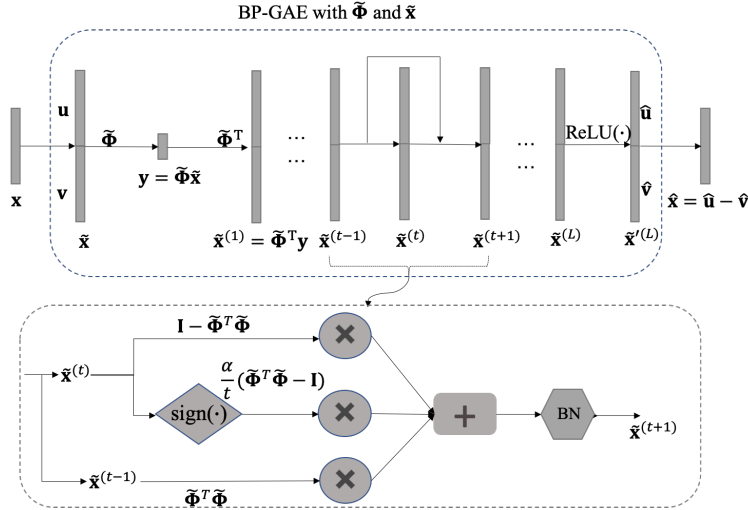


Fig. 7: Structure diagram of BP-GAEcat; the module BN represents batch normalization

IV. NUMERICAL RESULTS

A. Experiment Setup

We consider a massive MIMO system having 256 antennas at the BS and a single antenna at the UE. We adopt the public DeepMIMO dataset [47] generated with the parameters summarized in Table I, where the chosen ‘O1’ ray-tracing scenario is an outdoor signal propagation setup produced by the accurate 3D ray-tracing simulator Wireless InSite [48]. We first construct the spatial channel for each user and obtain the dataset containing 54,481 spatial-domain channel vectors. We neglect the power leakages and transform the spatial channel vectors into the s -sparse

TABLE I: DeepMIMO Dataset Parameters

Parameters	Values
Ray-tracing senario	'O1'
Activate BS	BS 4
Activate users	Rows from R1200 to R1500
Number of BS antennas	$M_x = 256$
Antenna spacing (in wavelength)	0.5
System bandwidth	0.5 GHz
Number of OFDM subcarriers	1024
OFDM sampling factor	1
OFDM limit	1
Number of channel paths	3

beamspace channel vectors with the sparsity level $s = 3$, which means we only care about the nonzero elements with largest-three magnitudes in the beamspace channel vectors. We split and stack the real part and imaginary part of the complex beamspace channel vectors in column-wise, thus we obtain the dataset containing 108,962 real-form sparse vectors. We normalize each sample in the dataset before training such that the performance is independent of the path loss, i.e., $\|\mathbf{x}\|_2 = 1$. The depth of decoder is set to be 15 layers, i.e., $L = 15$. The measurement matrix Φ is initialized by the truncated normal distribution with standard deviation $\sigma = 1/\sqrt{256}$. The step size parameter α as a trainable variable is initialized as $\alpha = 1.0$, and its value will be automatically updated to an appropriate value during training. The SGD is used as the optimizer for training the autoencoders. The training parameter settings and time consumption are summarized in the Appendix. The experiments ⁴ are repeated with different compressed dimensions M , which is taken from 6 to 30 with the interval three.

B. Reconstruction Errors for the Proposed Autoencoders

The proposed autoencoder models are evaluated by the reconstruction errors over the test dataset, and the reconstruction root mean square error (RMSE) ⁵ for different compressed dimension M are shown in Fig. 8. We first compare the BP-SAE and BP-GAE, and we can see

⁴Our experiment implementation is open to public at <https://github.com/Pengxia-Wu/DeepBP-AE>. Our dataset is open-access on IEEEDataPort with the DOI: 10.21227/n4eq-ft29.

⁵The RMSE is defined as the square root of $\mathbb{E}[\|\mathbf{x} - \hat{\mathbf{x}}\|_2^2]$.

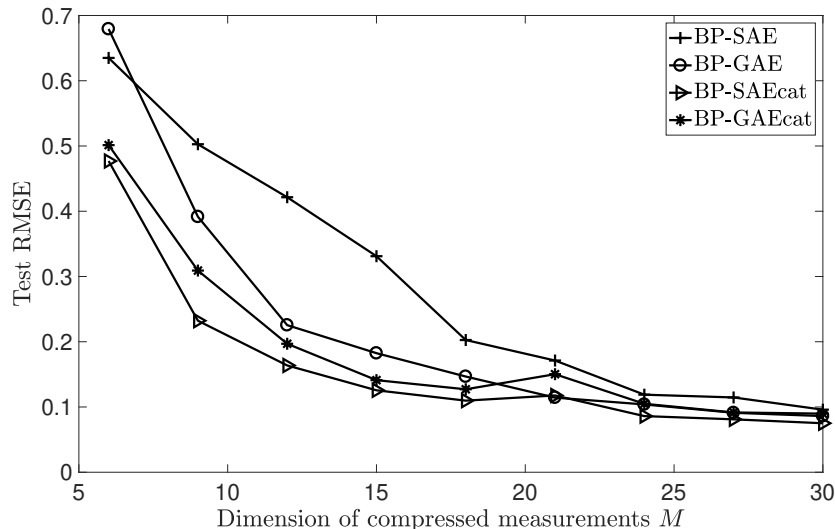


Fig. 8: Reconstruction RMSE over test dataset of the trained autoencoders

that the BP-GAE has a lower test error compared with the BP-SAE. This result confirms the proposed residual learning module, namely the term $\Phi^T \Phi \mathbf{x}^{(t-1)}$ in (18), can significantly improve the data fitting ability of the autoencoder. Then we turn to the extension models. The BP-SAEcat and BP-GAEcat have comparable reconstruction performance, and both of them have better reconstruction accuracy than BP-SAE and BP-GAE. This result indicates the better fitting abilities of the proposed extension models BP-SAEcat and BP-GAEcat than BP-SAE and BP-GAE. This performance improvement mostly benefits from the larger-size measurement matrix and the introduced nonnegativity constraint on the intermediate variable $\tilde{\mathbf{x}} \geq 0$ in BP-SAEcat and BP-GAEcat. Unfortunately, the results in Fig. 8 of reconstruction RMSE over test dataset indicate the reconstruction accuracies of all the autoencoders are overall unsatisfactory. The reason is that these autoencoder models aim to provide overall fitting for the whole dataset, and consequently they often cannot reconstruct every individual sample accurately. However, as will be shown in the following, we can incorporate the data-driven measurement matrices obtained from these trained autoencoders with classical reconstruct algorithms such as the linear programming to provide satisfactory reconstructions.

C. Reconstruction Performance Comparisons of the Data-Driven Matrices and Random Matrices with Linear Programming Recovery

We use $\Phi_{sae} \in \mathbb{R}^{M \times N}$, $\Phi_{gae} \in \mathbb{R}^{M \times N}$, $\tilde{\Phi}_{saec} \in \mathbb{R}^{M \times 2N}$ and $\tilde{\Phi}_{gaec} \in \mathbb{R}^{M \times 2N}$ to denote the learned matrices by BP-SAE, BP-GAE, BP-SAEcat and BP-GAEcat, respectively. We adopt the linear programming to solve the ℓ_1 -minimization sparse reconstruction (12) over the test dataset using different measurement matrices. Reconstruction performances of the data-driven measurement matrices are evaluated and compared with random matrices for different compressed dimension M . Four random matrices are adopted as baselines, including the random Gaussian matrix \mathbf{G} , the random Bernoulli matrix \mathbf{B} ⁶, the partial Fourier matrix \mathbf{F} , and the random selection matrix \mathbf{S} ⁷. Metrics for evaluating the reconstruction performances include the RMSE and the accurate reconstruction percentage. The reconstruction percentage is calculated as the ratio of the number of accurate reconstructed samples over the total number of samples in test dataset. A sample is considered to be reconstructed accurately if its reconstruction ℓ_2 -error is not more than 10^{-8} , i.e., $\|\mathbf{x} - \hat{\mathbf{x}}\|_2 \leq 10^{-8}$. The results of reconstruction RMSE are shown in Fig. 9 and the results of accurate reconstruction percentages are shown in Table II. The effective achievable rates for various measurement matrices are compared and shown in Fig. 10.

Performance comparisons with random matrices: From the Fig. 9, we can see the overall reconstruction errors of the data-driven matrices are significantly lower than the random matrices. From Table II, we can see the data-driven measurement matrices exhibit obvious higher accurate reconstruction percentages, especially for small compressed dimensions. For example, when the compressed dimension $M = 6$, the learned matrices $\tilde{\Phi}_{saec}$ and $\tilde{\Phi}_{gaec}$ can achieve over 50% accurate recoveries, whereas the percentages for random matrices are all almost zero. When $M = 9$ the data-driven matrices $\tilde{\Phi}_{saec}$ and $\tilde{\Phi}_{gaec}$ achieve over 90% accurate reconstruction percentage, while the accurate reconstruction percentages of random matrices are below 11%. We can also see the data-driven matrix can achieve accurate reconstructions using fewer measurements. For example, for the 95% threshold of accurate reconstruction percentage, the least number of required measurements is $M = 12$ by the matrices $\tilde{\Phi}_{saec}$ and $\tilde{\Phi}_{gaec}$. The matrix Φ_{gae} achieves 94.3%, which is almost 95% accurate reconstruction percentage when $M = 12$. However, the least number of required measurements is $M = 24$ for the random matrices. We can

⁶For random Bernoulli matrix, entries are -1 or 1 with equal probability.

⁷For random selection matrix, entries are 0 or 1 with equal probability.

see using data-driven matrix can save two-fold measurements, which is also four-fold sparsity level in our experiment setup.

Performance comparisons between data-driven matrices: The group of solid lines in Fig. 9 shows the average reconstruction RMSE for data-driven matrices. We can see the matrices $\tilde{\Phi}_{saec}$ and $\tilde{\Phi}_{gaec}$ show the lower reconstruction errors than the matrices Φ_{sae} and Φ_{gae} . The matrix Φ_{gae} achieves lower reconstruction errors than the matrix Φ_{sae} ; the matrix $\tilde{\Phi}_{saec}$ and $\tilde{\Phi}_{gaec}$ have almost equivalent reconstruction accuracies. The similar patterns can also be observed in Table II in terms of the accurate reconstruction percentages. We can see the matrices $\tilde{\Phi}_{saec}$ and $\tilde{\Phi}_{gaec}$ show higher accurate reconstruction percentages than the the matrices Φ_{sae} and Φ_{gae} in the low compressed dimension range for $6 \leq M \leq 12$; the matrix $\tilde{\Phi}_{saec}$ and the matrix $\tilde{\Phi}_{gaec}$ have comparable performances. We also notice that the matrix Φ_{gae} achieves noticeable improved reconstruction performances than the matrix Φ_{sae} both in Fig. 9 and Table II. For example, in Table II when $M = 12$ the accurate reconstruction percentage is 72.7% for matrix Φ_{sae} and is 84.7% for matrix Φ_{gae} . Although the matrix $\tilde{\Phi}_{saec}$ and $\tilde{\Phi}_{gaec}$ have overall better reconstruction performances, their sizes should be considered in practical applications. The matrices $\tilde{\Phi}_{saec}$ and $\tilde{\Phi}_{gaec}$ in the size of $M \times 2N$ can be used in compressed CSI feedback, but they are unsuitable for downlink pilot design. The matrices Φ_{sae} and Φ_{gae} of the size $M \times N$ are suitable for downlink pilot designs. The downlink pilot matrix requires the size $M \times N$ to match the unknown channel vectors of the size $N \times 1$, whereas for compressed CSI feedback the UE can transform the known beamspace channel vectors into $\tilde{\mathbf{x}} = [(\mathbf{x})_+^T, (-\mathbf{x})_+^T]^T$ in the size of $2N \times 1$, then use the measurement matrix of the size $M \times 2N$ to compress the channel vectors for feedback.

Achievable rate comparisons: A larger compressed dimension M will lead to more accurate reconstructions, but a lower spectrum efficiency. To analyze the trade-off between the dimension of measurements M and the recovery accuracy, we define the effective achievable rate as $R_e = R_0(1 - \frac{M}{B})P$ [15], where R_0 is the maximal achievable rate for a user, $\frac{M}{B}$ is the pilot occupation ratio in transmission block, B is the block length which is set as 50 symbols, and P is the probability of successful recoveries. As shown in Fig. 10, the effective achievable rates for data-driven matrices are shown in solid lines, while the effective achievable rates for random matrices are shown in dotted lines. We can see the maximum effective achievable rates of data-driven matrices are higher than random matrices. The effective achievable rate attains the maximum at $M = 9$ using the data-driven matrix $\tilde{\Phi}_{saec}$ and the matrix $\tilde{\Phi}_{gaec}$. The matrix Φ_{gae} achieves its maximum effective achievable rate at $M = 12$, and the matrix Φ_{sae} achieves its maximum

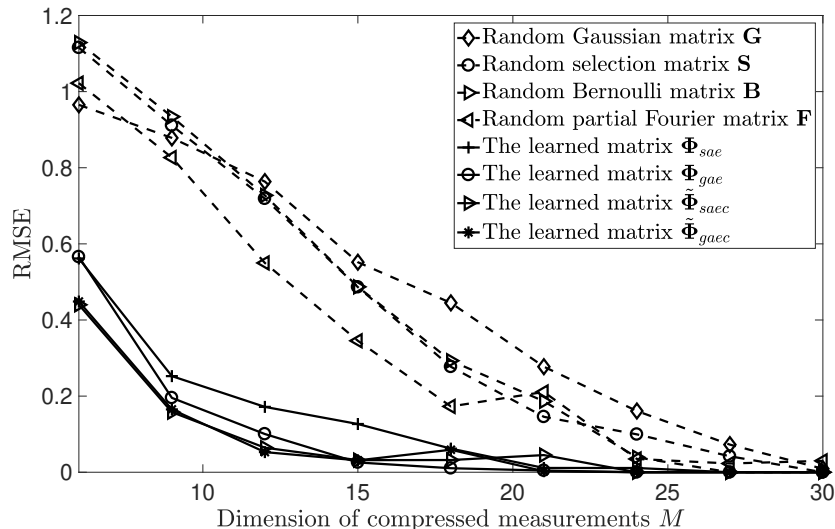


Fig. 9: Reconstruction RMSE of the measurement matrices

TABLE II: Accurate reconstruction percentages of various measurement matrices for different compressed dimension M with the reconstruction ℓ_2 -error threshold 10^{-8}

accurate reconstruct percentage matrix	$M = 6$	$M = 9$	$M = 12$	$M = 15$	$M = 18$	$M = 21$	$M = 24$	$M = 27$	$M = 30$
Gaussian matrix \mathbf{G}	0.0%	0.5%	4.2%	25.9%	47.7%	71.8%	90.7%	97.6%	99.9%
Bernoulli matrix \mathbf{B}	0.0%	2.5%	14.9%	44.4%	76.2%	89%	99.3%	100%	100%
Partial Fourier matrix \mathbf{F}	0.0%	10.4%	21.3%	75.4%	91.5%	89.4%	99.6%	99.8%	99.9%
Selection matrix \mathbf{S}	0.2%	2.1%	13%	42.3%	75.9%	92.1%	96.9%	98.7%	100%
Data-driven matrix Φ_{sae}	30.3%	72.7%	86.4%	92.4%	96.9%	99.5%	99.7%	100%	100%
Data-driven matrix Φ_{gae}	35.9%	84.7%	94.3%	99.3%	99.4%	99.9%	100%	100%	100%
Data-driven matrix $\tilde{\Phi}_{saec}$	52.5%	91.6%	97.2%	98.8%	99.2%	99.2%	100%	100%	100%
Data-driven matrix $\tilde{\Phi}_{gaec}$	52.9%	90.5%	97%	98.4%	97.6%	99.9%	100%	100%	100%

effective achievable rate at $M = 15$. For random matrices, the maximum effective achievable rates occurs around $M = 18$ or $M = 21$, and the maximum effective achievable rates are lower than the rates achieved by the data-driven matrices.

In summary, based on the comparisons of RMSE in Fig. 9 and accurate reconstruction percentages in Table II, we claim the data-driven matrices can achieve the lower average reconstruction errors and higher accurate reconstruction percentages than random matrices for

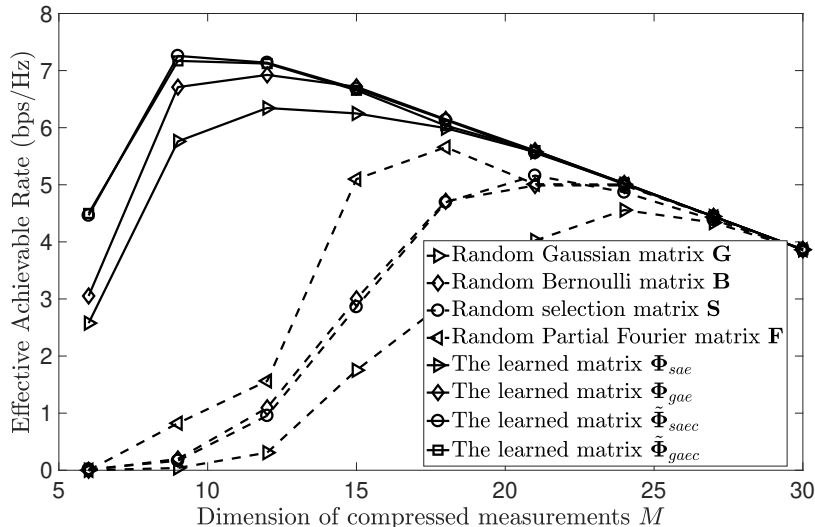


Fig. 10: Effective achievable rate using different measurement matrices

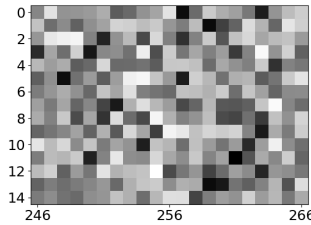
the same compressed dimension M . In other words, fewer measurements are required to attain a high level reconstruction accuracy when using the data-driven measurement matrices. This is meaningful for pilot and feedback overhead reduction in CSI acquisitions for mmWave massive MIMO systems. As shown in the comparisons of effective achievable rates in Fig. 10, using the data-driven measurement matrices can significantly improve the effective achievable rate. Considering the reconstruction performances, the computation complexities as well as the dimension requirements of measurement matrices in different application scenarios, the data-driven matrices $\tilde{\Phi}_{saec}$ acquired by BP-SAEcat is recommended for compressed CSI feedback, while the data-driven matrices Φ_{gae} acquired by BP-GAE is recommended for the downlink pilot design.

D. Experiment with Manually Structured Dataset

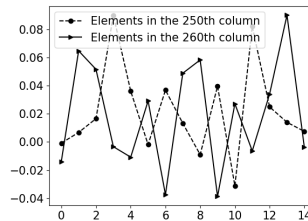
To show visually the data adaption of the data-driven matrices, we manually construct a toy dataset that has obvious structural feature. We randomly generate 20,000 spatial-domain channel realizations according to the channel model in (1), where the number of scattering clusters



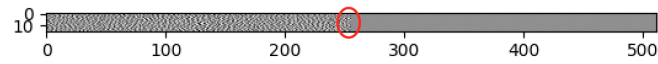
(a) Greyscale illustration of a Gaussian random matrix \mathbf{G} as the initialization matrix



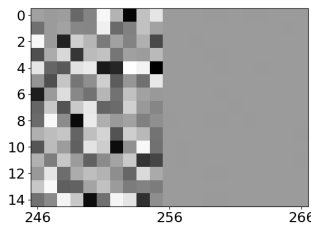
(b) Zoom in circled part of \mathbf{G}



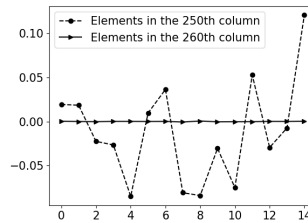
(c) Plot of sample columns of \mathbf{G}



(d) Greyscale illustration of the data-driven matrix Φ'_{sae} learned by BP-SAE



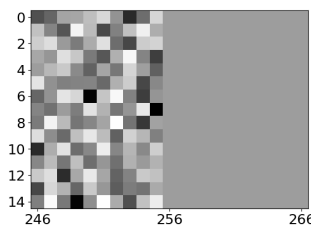
(e) Circled part zoom in of Φ'_{sae}



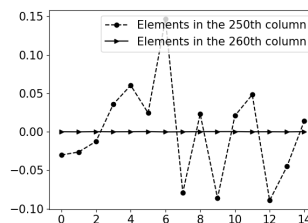
(f) Plot of sample columns of Φ'_{sae}



(g) Greyscale illustration of the data-driven matrix Φ'_{gae} learned by BP-GAE



(h) Zoom in circled part of Φ'_{gae}



(i) Plot of sample columns of Φ'_{gae}

Fig. 11: The visual illustration of Gaussian matrix \mathbf{G} , the data-driven matrix Φ'_{sae} learned by BP-SAE and data-driven matrix Φ'_{gae} learned by BP-GAE.

is set to be three⁸ and the AoDs of scattering clusters follow Uniform distribution between $[-\pi/2, \pi/2]$. We transform the generated spatial-domain channel vectors into beamspace channel vectors $\mathbf{x}' \in \mathbb{R}^{256}$, where the sparsity level is set to be three, i.e., $s = 3$. Then, we concatenate the beamspace channel vectors $\mathbf{x}' \in \mathbb{R}^{256}$ with all-zero vectors in the same size. Consequently, the samples in the new dataset can be represented as the vector $\mathbf{x}_c = [\mathbf{x}'^T, \mathbf{0}^T]^T$, where $\mathbf{x}_c \in \mathbb{R}^{512}$, $\mathbf{x}' \in \mathbb{R}^{256}$ and the all-zero vector $\mathbf{0}$ has length 256. We use the manually structured dataset to train the proposed autoencoders BP-SAE and BP-GAE, and visually illustrate the learned data-driven measurement matrix. The compressed dimension is set as $M = 15$. In the training, we initialize the trainable measurement matrix by the Gaussian matrix $\mathbf{G} \in \mathbb{R}^{15 \times 512}$ in which the elements follow standard Gaussian distribution with row-wise normalization. After training, the data-driven matrix learned by BP-SAE is denoted as $\Phi'_{sae} \in \mathbb{R}^{15 \times 512}$; the data-driven matrix learned by BP-GAE is denoted as $\Phi'_{gae} \in \mathbb{R}^{15 \times 512}$. The modified vector samples $\mathbf{x}_c \in \mathbb{R}^{512}$ are composed by two obviously distinct parts, the first-half being the sparse channel vector \mathbf{x}' and second-half being all zeros $\mathbf{0}$. The learned matrices are expected to produce more elements having larger absolute values in the first 256 columns.

The illustrations for the Gaussian matrix \mathbf{G} , the learned matrix Φ'_{sae} and the learned matrix Φ'_{gae} are shown in Fig. 11. The greyscale images for the matrix \mathbf{G} , Φ'_{sae} and Φ'_{gae} are shown in Fig. 11(a), Fig. 11(d) and Fig. 11(g), respectively. We can observe the greyscale for Gaussian matrix \mathbf{G} is in a uniform style, while the greyscales for the learned matrices Φ'_{sae} and Φ'_{gae} show different patterns for the first-half and second-half columns. To show clearly the difference, we zoom in the columns between the 246th column and the 266th column. The zoom-in images for the matrix \mathbf{G} , Φ'_{sae} and Φ'_{gae} are shown in Fig. 11(b), Fig. 11(e) and Fig. 11(h), respectively. Each small grey square represents an element in the matrix, and different grey-scaled colors indicate different values of the element, and the darker color means larger value. In Fig. 11(e) and Fig. 11(h), the columns from the 246th to the 256th column have distinct-valued elements, while the columns from the 256th to the 266th column show a same value. To illustrate further the values, we choose the 250th column and the 260th column in first-half and second-half columns respectively, and plot their element values. The plots of the sample columns for the

⁸More specifically, the scattering clusters include one line-of-sight path and two non-line-of-sight path; the Ricean K-factor is set to be 13.2dB; the complex path gains follow zero-mean Gaussian distribution; the number of antennas at the BS is set to be 256.

TABLE III: Accurate reconstruction percentages and RMSE with the Gaussian matrix \mathbf{G} and the data-driven matrix Φ'_{sae} , Φ'_{gae} for compressed dimension $M = 15$

Matrix	reconstruction percentage	RMSE
Gaussian matrix \mathbf{G}	12.4%	0.6
Data-driven matrix Φ'_{sae}	93.67%	0.09
Data-driven matrix Φ'_{gae}	96%	0.07

matrix \mathbf{G} , Φ'_{sae} and Φ'_{gae} are shown in Fig. 11(c), Fig. 11(f) and Fig. 11(i), respectively. With initializing with the values shown in Fig. 11(c), the two columns are optimized being the values shown in Fig. 11(f) and Fig. 11(i) after training by the autoencoders BP-SAE and BP-GAE. We can see that, the 260th columns for Φ'_{sae} and Φ'_{gae} are all zero-valued, which infers the second-half columns from the 256th to the 512th column are all-zeros. This result indicates the learned matrices can adapt to our manually structured features of the dataset. The all-zero columns of the learned measurement matrices are adaptive with the all-zero elements of the concatenating vectors $\mathbf{x}_c = [\mathbf{x}', \mathbf{0}]^T$. We evaluate the reconstruction performances of the Gaussian matrix \mathbf{G} , the learned matrix Φ'_{sae} and Φ'_{gae} , and compare the performances in Table III. We can see that the reconstruction accuracies are improved from 12.4% for the Gaussian matrix \mathbf{G} to 93.67% for the matrix Φ'_{sae} and 96% for the matrix Φ'_{gae} , and the RMSE are decreased from 0.6 for the Gaussian matrix \mathbf{G} to 0.09 for the matrix Φ'_{sae} and 0.07 for the matrix Φ'_{gae} . The learned data-adaptive matrices Φ'_{sae} and Φ'_{gae} have significantly improved reconstruction performances compared with the initializing Gaussian matrix \mathbf{G} .

V. CONCLUSION

We proposed a data-driven approach for acquiring the measurement matrix. To acquire the data-driven measurement matrix, we considered a generic deep BP-AE framework consisting of a linear dimension-reduction encoder and a stack layers of decoder mimicking the basis pursuit reconstruction algorithm. Under this framework, we constructed two model-based autoencoders BP-SAE and BP-GAE which are parameterized with the measurement matrix. The proposed autoencoders were trained to acquire the data-driven measurement matrices for sparse beamspace channel vectors. The acquired data-driven matrices can attain higher achievable rate compared with conventional random matrices, because more accurate reconstructions can be accomplished using fewer measurements by data-driven measurement matrices. The acquired

data-driven measurement matrices work excellently with traditional linear programming sparse recovery algorithm, and can be applied to the pilot design or the feedback CSI compression to reduce the overheads of downlink pilot training and CSI feedback. This work provides an example of incorporating the data-driven method to improve the traditional compressed sensing schemes, and demonstrates a useful application of deep learning techniques for designing mmWave massive MIMO systems. For future work, we will consider the data-driven measurement matrix design in noisy scenarios where the measurements are corrupted by noise and quantization errors.

APPENDIX

TABLE IV: Number of training epoches (epoches)

	BP-SAE	BP-GAE	BP-SAEcat	BP-GAEcat
$M = 6$	16	16	31	16
$M = 9$	41	41	106	46
$M = 12$	16	61	116	81
$M = 15$	26	51	116	116
$M = 18$	76	66	166	151
$M = 21$	121	121	131	121
$M = 24$	176	171	161	131
$M = 27$	121	116	221	186
$M = 30$	211	116	261	146

TABLE V: Training time in seconds (secs)

	BP-SAE	BP-GAE	BP-SAEcat	BP-GAEcat
$M = 6$	27	49	80	102
$M = 9$	68	120	303	301
$M = 12$	27	177	342	535
$M = 15$	45	149	351	777
$M = 18$	137	198	520	1049
$M = 21$	217	373	387	839
$M = 24$	316	524	473	909
$M = 27$	226	368	674	1332
$M = 30$	395	372	786	1066

The autoencoder training was performed on a desktop computer equipped with 3.2 GHz Intel Core i7-8700 CPU. Training parameters were set as follows: learning rate was 0.01; batch size

was 128; the maximum number of training epoches⁹ was set as 1,000. We checked reconstruction errors every five epoches over the validation dataset. The tolerance number of training epoches was set as five for early stopping, which means the training will be stopped if the results of the validation error are not getting better within the tolerance number of epochs. To reduce the training time, we did not use the whole dataset for each training. Instead, for each training we shuffled the whole dataset and only use 50,000 samples. We split the 50,000 samples into training, validation, and test set by the ratio of 0.96/0.02/0.02. The training time and epoches, which depend on compressed dimension M , are summarized in Table IV and Table V.

REFERENCES

- [1] A. L. Swindlehurst, E. Ayanoglu, P. Heydari, and F. Capolino, "Millimeter-wave massive MIMO: The next wireless revolution?" *IEEE Commun. Mag.*, vol. 52, no. 9, pp. 56–62, Sep. 2014.
- [2] A. F. Molisch, V. V. Ratnam, S. Han, Z. Li, S. L. H. Nguyen, L. Li, and K. Haneda, "Hybrid beamforming for massive MIMO: A survey," *IEEE Commun. Mag.*, vol. 55, no. 9, pp. 134–141, Sep. 2017.
- [3] R. W. Heath, N. Gonzalez-Prelcic, S. Rangan, W. Roh, and A. M. Sayeed, "An overview of signal processing techniques for millimeter wave MIMO systems," *IEEE J. Sel. Topics Signal Process.*, vol. 10, no. 3, pp. 436–453, Apr. 2016.
- [4] J. W. Choi, B. Shim, Y. Ding, B. Rao, and D. I. Kim, "Compressed sensing for wireless communications: Useful tips and tricks," *IEEE Commun. Surveys Tut.*, vol. 19, no. 3, pp. 1527–1550, Third Quart. 2017.
- [5] W. U. Bajwa, J. Haupt, A. M. Sayeed, and R. Nowak, "Compressed channel sensing: A new approach to estimating sparse multipath channels," *Proc. IEEE*, vol. 98, no. 6, pp. 1058–1076, June 2010.
- [6] Z. Gao, L. Dai, W. Dai, B. Shim, and Z. Wang, "Structured compressive sensing-based spatio-temporal joint channel estimation for FDD massive MIMO," *IEEE Trans. Commun.*, vol. 64, no. 2, pp. 601–617, Feb. 2016.
- [7] X. Rao and V. K. N. Lau, "Distributed compressive CSIT estimation and feedback for FDD multi-user massive MIMO systems," *IEEE Trans. Signal Process.*, vol. 62, no. 12, pp. 3261–3271, June 2014.
- [8] Z. Gao, L. Dai, Z. Wang, and S. Chen, "Spatially common sparsity based adaptive channel estimation and feedback for FDD massive MIMO," *IEEE Trans. Signal Process.*, vol. 63, no. 23, pp. 6169–6183, Dec. 2015.
- [9] W. Shen, L. Dai, Y. Shi, B. Shim, and Z. Wang, "Joint channel training and feedback for FDD massive MIMO systems," *IEEE Trans. Veh. Technol.*, vol. 65, no. 10, pp. 8762–8767, Oct. 2016.
- [10] X. Li, J. Fang, H. Li, and P. Wang, "Millimeter wave channel estimation via exploiting joint sparse and low-rank structures," *IEEE Trans. Wireless Commun.*, vol. 17, no. 2, pp. 1123–1133, Feb. 2018.
- [11] X. Lin, S. Wu, C. Jiang, L. Kuang, J. Yan, and L. Hanzo, "Estimation of broadband multiuser millimeter wave massive MIMO-OFDM channels by exploiting their sparse structure," *IEEE Trans. Wireless Commun.*, vol. 17, no. 6, June 2018.
- [12] X. Gao, L. Dai, S. Han, C. I, and X. Wang, "Reliable beamspace channel estimation for millimeter-wave massive MIMO systems with lens antenna array," *IEEE Trans. Wireless Commun.*, vol. 16, no. 9, pp. 6010–6021, Sep. 2017.
- [13] Z. Gao, C. Hu, L. Dai, and Z. Wang, "Channel estimation for millimeter-wave massive MIMO with hybrid precoding over frequency-selective fading channels," *IEEE Commun. Lett.*, vol. 20, no. 6, pp. 1259–1262, June 2016.

⁹An epoch refers to a full pass of the training algorithm over the entire training dataset.

- [14] Z. Gao, L. Dai, and Z. Wang, "Channel estimation for mmWave massive MIMO based access and backhaul in ultra-dense network," in *Proc. 2016 IEEE Int. Conf. Commun. (ICC)*, May 2016, pp. 1–6.
- [15] A. Alkhateeb, G. Leus, and R. W. Heath, "Compressed sensing based multi-user millimeter wave systems: How many measurements are needed?" in *Proc. IEEE Int. Conf. Acoust. Speech Signal Process.*, Apr. 2015, pp. 2909–2913.
- [16] Z. Liu, S. Sun, Q. Gao, and H. Li, "CSI feedback based on spatial and frequency domains compression for 5G multi-user massive MIMO systems," in *2019 IEEE/CIC International Conference on Communications in China (ICCC)*, Aug. 2019, pp. 834–839.
- [17] J. Shen, J. Zhang, E. Alsusa, and K. B. Letaief, "Compressed CSI acquisition in FDD massive MIMO: How much training is needed?" *IEEE Trans. Wireless Commun.*, vol. 15, no. 6, pp. 4145–4156, June 2016.
- [18] H. Song, W. Seo, and D. Hong, "Compressive feedback based on sparse approximation for multiuser MIMO systems," *IEEE Trans. Veh. Technol.*, vol. 59, no. 2, pp. 1017–1023, Feb. 2010.
- [19] C. R. Berger, Z. Wang, J. Huang, and S. Zhou, "Application of compressive sensing to sparse channel estimation," *IEEE Commun. Mag.*, vol. 48, no. 11, pp. 164–174, Nov. 2010.
- [20] Z. Qin, J. Fan, Y. Liu, Y. Gao, and G. Y. Li, "Sparse representation for wireless communications: A compressive sensing approach," *IEEE Signal Process. Mag.*, vol. 35, no. 3, May 2018.
- [21] R. DeVore, "Deterministic constructions of compressed sensing matrices," *Journal of Complexity*, vol. 23, pp. 918–925, 2007.
- [22] J. Bourgain, S. Dilworth, K. Ford, S. Konyagin, and D. Kutzarova, "Explicit constructions of RIP matrices and related problems," *Duke Mathematical Journal*, vol. 159, p. 145185, 2011.
- [23] Z. Xu, "Deterministic sampling of sparse trigonometric polynomials," *Journal of Complexity*, vol. 27, pp. 133–140, 2011.
- [24] R. Obermeier and J. A. Martinez-Lorenzo, "Sensing matrix design via mutual coherence minimization for electromagnetic compressive imaging applications," *IEEE Trans. Comput. Imag.*, vol. 3, no. 2, pp. 217–229, June 2017.
- [25] M. Lotfi and M. Vidyasagar, "A fast noniterative algorithm for compressive sensing using binary measurement matrices," *IEEE Trans. Signal Process.*, vol. 66, no. 15, pp. 4079–4089, Aug. 2018.
- [26] J. L. R. J. Hershey and F. Wening, "Deep unfolding: Model-based inspiration of novel deep architectures," *arXiv preprint, arXiv:1409.2574*, 2014.
- [27] D. L. Donoho, "Compressed sensing," *IEEE Trans. Inform. Theory*, vol. 52, no. 4, pp. 1289–1306, Apr. 2006.
- [28] S. Wu, A. G. Dimakis, S. Sanghavi, F. X. Yu, D. Holtmann-Rice, D. Storch, A. Rostamizadeh, and S. Kumar, "Learning a compressed sensing measurement matrix via gradient unrolling," in *Proceedings of the 36th International Conference on Machine Learning (PMLR)*, 2019, pp. 6828–6839.
- [29] C. K. Wen, W. T. Shih, and S. Jin, "Deep learning for massive MIMO CSI feedback," *IEEE Wireless Commun. Lett.*, vol. 7, no. 5, pp. 748–751, Oct. 2018.
- [30] T. Wang, C. Wen, S. Jin, and G. Y. Li, "Deep learning-based CSI feedback approach for time-varying massive MIMO channels," *IEEE Wireless Commun. Lett.*, vol. 8, no. 2, pp. 416–419, Apr. 2019.
- [31] H. He, C. Wen, S. Jin, and G. Y. Li, "Deep learning-based channel estimation for beamspace mmWave massive MIMO systems," *IEEE Wireless Commun. Lett.*, vol. 7, no. 5, pp. 852–855, Oct. 2018.
- [32] C. Lu, W. Xu, H. Shen, J. Zhu, and K. Wang, "MIMO channel information feedback using deep recurrent network," *IEEE Commun. Lett.*, vol. 23, no. 1, pp. 188–191, Jan. 2019.
- [33] Y. Jang, G. Kong, M. Jung, S. Choi, and I. Kim, "Deep autoencoder based CSI feedback with feedback errors and feedback delay in FDD massive MIMO systems," *IEEE Wireless Commun. Lett.*, vol. 8, no. 3, pp. 833–836, June 2019.
- [34] Z. Liu, L. Zhang, and Z. Ding, "Exploiting bi-directional channel reciprocity in deep learning for low rate massive MIMO CSI feedback," *IEEE Wireless Commun. Lett.*, vol. 8, no. 3, pp. 889–892, June 2019.

- [35] C.-J. Chun, J.-M. Kang, and I.-M. Kim, "Deep learning-based channel estimation for massive MIMO systems," *IEEE Commun. Lett.*, vol. 8, no. 4, pp. 1228–1231, Aug. 2019.
- [36] —, "Deep learning-based joint pilot design and channel estimation for multiuser MIMO channels," *IEEE Commun. Lett.*, vol. 23, no. 11, pp. 1999–2003, Nov. 2019.
- [37] J. Brady, N. Behdad, and A. M. Sayeed, "Beamspace MIMO for millimeter-wave communications: System architecture, modeling, analysis, and measurements," *IEEE Trans. Antennas Propag.*, vol. 61, no. 7, pp. 3814–3827, July 2013.
- [38] E. J. Candes and T. Tao, "Decoding by linear programming," *IEEE Trans. Inform. Theory*, vol. 51, no. 12, pp. 4203–4215, Dec 2005.
- [39] E. J. Candes, J. K. Romberg, and T. Tao, "Stable signal recovery from incomplete and inaccurate measurements," *Commun. Pure Appl. Math.*, vol. 59, no. 8, pp. 1207–1223, Aug. 2006.
- [40] A. Cohen, W. Dahmen, and R. DeVore, "Compressed sensing and best k-term approximation," *The Journal of the American Mathematical Society (JAMS)*, no. 1, pp. 211–231, Jan. 2009.
- [41] T. T. Cai and A. Zhang, "Sparse representation of a polytope and recovery of sparse signals and low-rank matrices," *IEEE Trans. Inform. Theory*, vol. 60, no. 1, pp. 122–132, Jan 2014.
- [42] Z. Qin, H. Ye, G. Y. Li, and B. F. Juang, "Deep learning in physical layer communications," *IEEE Wireless Commun.*, vol. 26, no. 2, pp. 93–99, Apr. 2019.
- [43] E. Amaldi and V. Kann, "On the approximability of minimizing nonzero variables or unsatisfied relations in linear systems," *Theoretical Computer Science*, vol. 209, pp. 237–260, 1998.
- [44] S. Boyd, L. Xiao, and A. Mutapcic, "Subgradient methods," *Notes for EE392o Stanford University Autumn, 2003-2004*.
- [45] K. He, X. Zhang, S. Ren, and J. Sun, "Deep residual learning for image recognition," in *Proceedings of the IEEE conference on computer vision and pattern recognition (CVPR)*, 2016, pp. 770–778.
- [46] P. Wu, Z. Liu, and J. Cheng, "Learning a measurement matrix in compressed CSI feedback for millimeter wave massive MIMO systems," *arXiv preprint, arXiv:1903.02127*, 2019.
- [47] A. Alkhateeb, *DeepMIMO: A Generic Deep Learning Dataset for Millimeter Wave and Massive MIMO Applications*. [Online]. Available: <https://www.deepmimo.net/>
- [48] —, "DeepMIMO: A generic deep learning dataset for millimeter wave and massive MIMO applications," in *Information Theory and Applications Workshop (ITA)*, San Diego, CA, Feb 2019, pp. 1–8.